Determination of the Fermi surface in high-T_c superconductors by angle-resolved photoemission spectroscopy

J. Mesot,[1,2,*] M. Randeria,[3] M. R. Norman,[1] A. Kaminski,[2,1] H. M. Fretwell,[2,†] J. C. Campuzano,[2,1] H. Ding,[4] T. Takeuchi,[5] T. Sato,[6] T. Yokoya,[6] T. Takahashi,[6] I. Chong,[7] T. Terashima,[7] M. Takano,[7] T. Mochiku,[8] and K. Kadowaki[9]

[1]*Materials Sciences Division, Argonne National Laboratory, Argonne, Illinois 60439*
[2]*Department of Physics, University of Illinois at Chicago, Chicago, Illinois 60607*
[3]*Tata Institute of Fundamental Research, Mumbai 400005, India*
[4]*Department of Physics, Boston College, Chestnut Hill, Massachusetts 02467*
[5]*Department of Crystalline Materials Science, Nagoya University, Nagoya 464-01, Japan*
[6]*Department of Physics, Tohoku University, 980-8578 Sendai, Japan*
[7]*Institute for Chemical Research, Kyoto University, Uji 611-0011, Japan*
[8]*National Research Institute for Metals, Sengen, Tsukuba, Ibaraki 305, Japan*
[9]*Institute of Materials Science, University of Tsukuba, Ibaraki 305, Japan*
(Received 25 October 1999; revised manuscript received 13 September 2000; published 23 May 2001)

We study the normal-state electronic excitations probed by angle-resolved photoemission spectroscopy (ARPES) in $Bi_{1.6}Pb_{0.4}Sr_2CuO_6$ (Bi2201) and $Bi_2Sr_2CaCu_2O_{8+\delta}$ (Bi2212). Our main goal is to establish explicit criteria for determining the Fermi surface from ARPES data on strongly interacting systems where sharply defined quasiparticles do not exist and the dispersion is very weak in parts of the Brillouin zone. Additional complications arise from strong matrix element variations within the zone. We present detailed results as a function of incident photon energy, and show simple experimental tests to distinguish between an intensity drop due to matrix element effects and spectral weight loss due to a Fermi crossing. We reiterate the use of polarization selection rules in disentangling the effect of umklapps due to the BiO superlattice in Bi2212. We conclude that, despite all the complications, the Fermi surface can be determined unambiguously; it is a single large hole barrel centered about (π, π) in both materials.

I. INTRODUCTION

The electronic structure and Fermi surfaces of conventional metals have been studied in great detail by ARPES.[1] The question of the determination of the Fermi surface[2–5] by ARPES in the normal state of the high T_c superconductors is of great interest, especially since other Fermi surface probes (like de Haas-van Alphen and positrons) have not yet yielded useful information on the Fermi surface of the planar Cu-O states. However, this question is not a trivial one, since these materials are strongly correlated, and likely not Fermi liquids, exhibiting very broad, ill-defined electronic excitations.[5,6]

The determination of the Fermi surface by ARPES in these systems is further complicated by the very small dispersion in the vicinity of the $(\pi,0)$ point of the Brillouin zone,[5,7,8] and by strongly **k**-dependent photoemission matrix elements, which lead to intensity variations that have nothing to do with Fermi crossings. Bi2212 has an additional complication: final-state diffraction of photoelectrons by the **Q** $=(0.21\pi,0.21\pi)$ structural modulation in the BiO layers.[5,9,10] The combination of all these effects, if not treated correctly, can be a source of confusion and lead to apparently contradictory conclusions,[8,11–13] even though the data between various groups are completely consistent with one another.

It is therefore important to establish the criteria for unambiguously extracting the Fermi surface from ARPES data. This is the main goal of the paper presented here, in which we study near optimal and overdoped samples of $Bi_2Sr_2CaCu_2O_{8+\delta}$ (Bi2212) and $Bi_{1.6}Pb_{0.4}Sr_2CuO_6$ (Bi2201) using a range of incident photon energies from 17–60 eV. Our extensive study leads us to the same conclusion as our previous work,[5,14] namely, that the Fermi surface consists of a single hole barrel centered around (π, π), the most antibonding point in the Brillouin zone. Furthermore, the Fermi surface is consistent with the Luttinger count with its volume scaling as one plus the number of doped holes.

The paper is organized as follows. In Sec. II, we describe the samples and experimental details. We begin with ARPES data over a wide (6 eV) scale describing the full valence band in Sec. III, and then turn to low energy, near E_F features in the rest of the paper. Section IV contains a brief description of polarization selection rules and their experimental implications. We then discuss in some detail criteria for determining the Fermi surface in Sec. V. In Sec. VI we present data on Bi2212 and Bi2201 and show how the various criteria proposed in Sec. V, fare in determining Fermi crossings. We find that the symmetrization method for inferring when the spectral function peak goes through the chemical potential is a very powerful tool and works even when the energy distribution curves (EDC's) are broad and weakly dispersive. We discuss in Secs. VII and VIII the usefulness and limitations of using the integrated intensity to determine $\mathbf{k}_F$, emphasizing the importance of the photon energy and **k** dependence of the ARPES matrix elements. By analyzing data obtained at different incident photon energies, we explicitly show how one can experimentally separate matrix
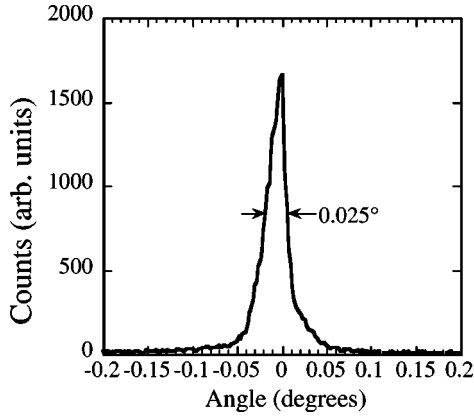
FIG. 1. Rocking curve of a (0,0,10) reflection on a Bi2212 sample showing the large structural coherence length.

element effects from those due to changes in the momentum distribution. In Sec. IX, we finally turn to the Fermi surface in Bi2212 where, in addition to all the issues discussed above for Bi2201, one also needs to be careful about BiO superlattice effects. Polarization selection rules are exploited to disentangle superlattice effects from the intrinsic CuO_2 electronic structure. We conclude in Sec. X.

An Appendix contains some further technical details related to the symmetrization procedure.

II. EXPERIMENTAL DETAILS

Our experiments are on very high quality single crystals of Bi2212 and Bi2201 grown by the traveling solvent floating zone method with an infrared mirror furnace, with low defect densities, as it can be appreciated from the high resolution x-ray diffraction rocking curve shown in Fig. 1. The samples are labeled by their doping levels (OPT for optimal doped and OD for overdoped) together with their onset T_c.

The as-grown Bi2212 samples are slightly overdoped and have $T_c = 87$ K with a transition width of 1K as determined by a superconducting quantum interference device magnetometer. These samples are most stable in terms of their photoemission characteristics. We look at Bi2201 samples in the doping range from OD 23 K to heavily OD 0 K. The samples are cleaved *in situ*, and have optically flat surfaces as measured by specular laser reflections. It is absolutely essential to characterize the flatness of the surface on which ARPES experiments are done. Another measure of the sample quality, within ARPES, is the observation of ''umklapp'' bands[5] in the electronic structure of Bi2212 samples, due to the presence of a structural superlattice modulation in the BiO layer. Since the structural superlattice has a periodicity of ~5 times the unit cell, very good long-range order is required for its observation.

The experiments were performed at the Synchrotron Radiation Center, Wisconsin, using a high-resolution 4-m normal incidence monochromator with a resolving power of 10^4 at 10^{11} photons/s. The samples are carefully oriented in the sample holder to an accuracy of 1° by Laue diffraction, and the orientation is further confirmed by the observed symme-
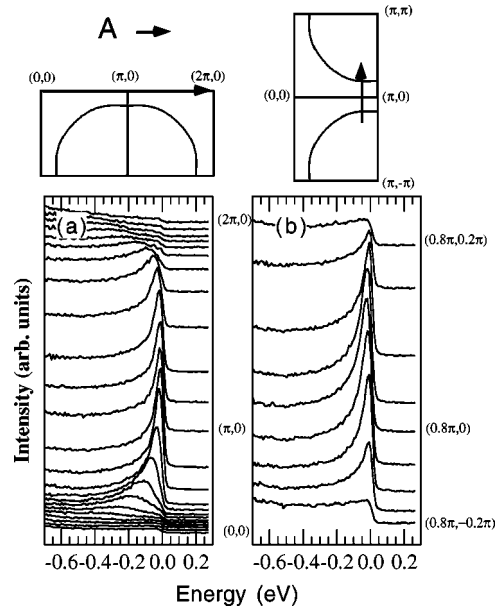
FIG. 2. Energy distribution curves (EDC's) obtained at $h\nu = 22$ eV for a Bi2201-OD 4 K sample, showing the symmetry about the $(0,0) \rightarrow (2\pi,0)$ (a) and the $(\pi,-\pi) \rightarrow (\pi,\pi)$ (b) directions.

try of sharp ARPES features around high-symmetry points, as described below.

Some of the data analyzed below (in particular Figs. 5, 12, 15, and 16) were obtained using a Scienta analyzer, at a variety of incident photon energies, with an energy resolution of 16 meV and a high **k** resolution better than 0.01 Å^{-1} at 22 eV photon energy. The detailed analysis presented in this paper leads to conclusions that are completely consistent with the recent high **k**-resolution results of our group[15] (emphasizing low-temperature data on Bi2212), as well as that of Borisenko *et al.*[16]

For the Brillouin zone of Bi2212 and Bi2201, we use a square lattice notation with $\Gamma\bar{M}$ along the CuO bond direction, as shown in the insets of Fig. 2. $\Gamma = (0,0)$, $\bar{M} = (\pi,0)$, $X = (\pi,-\pi)$, and $Y = (\pi,\pi)$ in units of $1/a^*$, where $a^* = 3.83$ Å is the separation between near neighbor Cu ions. (The orthorhombic *a* axis is along *X* and the *b* axis along *Y*.)

An example of how ARPES is used in sample alignment is shown in Fig. 2, where spectra are shown along the $(0,0)-(2\pi,0)$ and the $(\pi,\pi)-(\pi,-\pi)$ high-symmetry lines of the Brillouin zone. This symmetry is reflected in the position of the peak in the spectra in Fig. 2, and allows us to accurately find the surface normal, and the angle of the sample about this normal, completely determining the momentum **k** of the outgoing electron. Note that this alignment procedure only makes use of the symmetry properties of the peak positions,[17] and does not require a knowledge of the Fermi surface (indicated by the curves in the top panels of Fig. 2).

III. THE VALENCE BAND

Our main focus will be on near E_F electronic structure, but we begin with a brief discussion of angle-resolved pho-
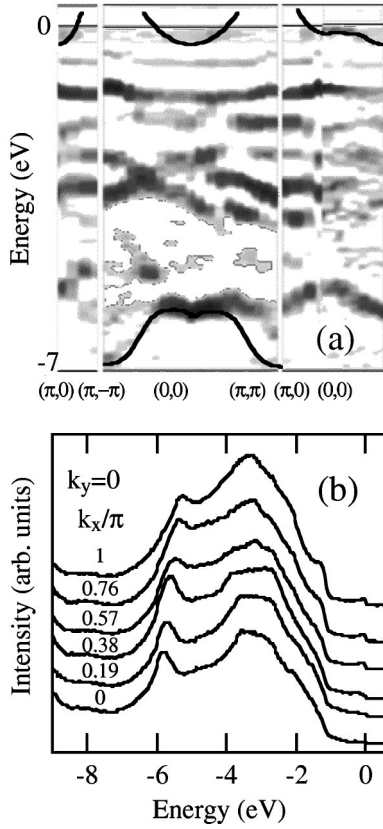
FIG. 3. (a)Electronic structure of the valence band of Bi2212 obtained by taking the second derivative of EDC's such as those shown in (b) at $h\nu = 22$ eV.

FIG. 4. (a)Arrangement of the photon beam and detector in order to make use of the photoemission selection rules. (b) Parity of the Cu$d_{x^2-y^2}$ orbitals hybridized with the O2p orbitals. (c) EDC's showing the parity of the orbitals in (b) obtained at $h\nu = 22$ eV.

toemission from the complete valence band of Bi2212. This covers an energy range of approximately 6 eV from the Fermi energy (the small peak near zero) to the bottom of the valence band. The electronic structure can be divided into three groups, as indicated in Fig. 3(a): the most bonding CuO$_2$ state is at the bottom of the valence band (the peak at 6 eV), the antibonding state is at the Fermi energy, and the nonbonding states are in between. The "lump" in the middle also includes states from elements in the structure other than Cu and O. But since these layers are insulating, the corresponding states do not cross the Fermi energy.

By varying the in-plane momentum **k**, one can map the complete electronic structure of the valence band, as shown in Fig. 3(a). These curves were obtained without fitting peaks to the data. Instead, the second derivative of the observed spectra, as shown in Fig. 3(b), was taken and plotted as a gray scale without any modifications.[18] Two considerations apply: the energy step in these spectra is only 30 meV, and therefore the details of the dispersion near the Fermi energy are not clear, and the spectra were obtained with a particular polarization of the photons, so that not all states show optimal intensity. Nonetheless, the most noteworthy features are the most bonding and antibonding states, highlighted by thick dark lines. In the remainder of the paper, we will focus exclusively on the antibonding states in the region near the Fermi energy.

IV. SELECTION RULES

We now focus on the states crossing the Fermi energy in Fig. 3(a) and show how one can determine the symmetry of the initial state in ARPES. The ARPES intensity is governed by the (square of the) dipole matrix element M_{fi} connecting the initial state $|\psi_i\rangle$ to the final state $|\psi_f\rangle$, given by $|\langle\psi_f|\mathbf{A}\cdot\mathbf{p}|\psi_i\rangle|^2$, where **A** is the vector potential of the (linearly polarized) incident photon, and **p** is the momentum operator.

We use a simple version of the selection rules proposed by Hermanson.[19] Let the photon beam be incident along a plane of mirror symmetry of the sample ($\mathcal{M}$). If the detector is placed in the same mirror plane as shown in Fig. 4(a), then the final state ψ_f must be even with respect to reflection in $\mathcal{M}$, because if it were odd the wave function would vanish at the detector. The dipole transition is allowed if the entire matrix element has an overall even symmetry. Thus two possibilities arise.[20] First, if the initial state ψ_i is even with respect to $\mathcal{M}$, then the light polarization **A** must also be even, i.e., parallel to $\mathcal{M}$. Second, if the initial state is odd with respect to $\mathcal{M}$, then **A** must also be odd, i.e., perpendicular to $\mathcal{M}$. This can be summarized as

$$\langle\psi_f|\mathbf{A}\cdot\hat{\mathbf{p}}|\psi_i\rangle\begin{cases}\psi_i\ even\ \langle+|+|+\rangle\Rightarrow & \mathbf{A}\ even,\\ \psi_i\ odd\ \langle+|-|-\rangle\Rightarrow & \mathbf{A}\ odd.\end{cases}\quad(1)$$

Consider hybridized Cu3$d-$O2p initial states, as shown in Fig. 4(b), which have a $d_{x^2-y^2}$ symmetry about a Cu site. These states are even with respect to $(0,0)-(\pi,0)$ (i.e., the plane defined by this symmetry axis and the z axis) and odd

with respect to $(0,0)-(\pi,\pi)$. Therefore, measurement along the $(0,0)-(\pi,0)$ direction will be dipole allowed (forbidden) if the polarization vector **A** is parallel (perpendicular) to this axis. Figure 4(c) shows that, consistent with an initial state, which is even about $(0,0)-(\pi,0)$, the signal is maximized when **A** lies in the mirror plane and minimized when **A** is perpendicular to this plane. (The reasons for nonzero intensity in the dipole forbidden geometry are the small, but finite, **k** window of the experiment and the possibility of a small misalignment of the sample.) Similarly, we have checked experimentally that (for Bi2212 in the Y quadrant where there are no superlattice complications) the initial state is consistent with odd symmetry about $(0,0)-(\pi,\pi)$.

While the dipole matrix elements are strongly photon energy dependent, the selection rules are, of course, independent of photon energy. This has been checked by measurements at 22 eV and 34 eV. All of these results are consistent with the fact that we are probing $Cu3d-O2p$ initial states with $d_{x^2-y^2}$ symmetry. In addition, as we shall emphasize below, the selection rules can be exploited to one's great advantage in disentangling the main CuO_2 ''band'' from its umklapp images due to the superlattice in Bi2212.

V. FERMI-SURFACE CRITERIA

Many criteria have been used for determining the Fermi surface in the past without a clear discussion of the conditions under which they are applicable. We will present three criteria here: (a) one based on dispersion of the EDC spectral peaks through the chemical potential, (b) a second one based on the peak of the spectral function inferred from symmetrized data, and (c) a third one based on rapid changes in the momentum distribution. In the following sections we will show how these criteria fare when applied to experimental data. Other criteria, not discussed in this paper, will be briefly alluded to at the end of this section.

The ARPES intensity is given by[21]

$$I(\mathbf{k},\omega)=I_0(\mathbf{k};\nu;\mathbf{A})f(\omega)A(\mathbf{k},\omega) \qquad (2)$$

for a quasi-two-dimensional (2D) system, assuming validity of the impulse approximation. Here **k** is the in-plane momentum, ω is the energy of the initial state measured relative to the chemical potential, $f(\omega)=1/[\exp(\omega/T)+1]$ is the Fermi function, and the one-particle spectral function $A(\mathbf{k},\omega)=(-1/\pi)\Im m G(\mathbf{k},\omega+i0^+)$. The prefactor I_0 is proportional to the dipole matrix element $|M_{fi}|^2$ and thus a function of **k** and of the incident photon energy $h\nu$ and polarization **A**. It is also important to remember that the experimentally observed EDC involves a convolution of the intensity of Eq. (2) with the energy resolution function and a sum over the momentum resolution window. There is also an additive (extrinsic) background contribution to the EDC, however this has little effect on Fermi surface determination since the background is negligible at the chemical potential.[22]

We first discuss the simplest case of noninteracting electrons that have infinitely sharp energy levels leading to a spectral function $A(\mathbf{k},\omega)=\delta(\omega-\epsilon_{\mathbf{k}})$. A Fermi-surface crossing $\mathbf{k}_F$ is then defined by the location in **k** space, where

the sharp peak of the spectral function crosses the chemical potential ($\omega=0$), i.e., $\epsilon_{\mathbf{k}_F}=0$. It is also useful to look at the momentum distribution

$$n(\mathbf{k})=\int_{-\infty}^{+\infty}d\omega f(\omega)A(\mathbf{k},\omega). \qquad (3)$$

For noninteracting electrons $n(\mathbf{k})=f(\epsilon_{\mathbf{k}})$, the Fermi function. At $T=0$ then, the momentum distribution shows a jump discontinuity at $\mathbf{k}_F$. At low temperatures there is no singularity in $n(\mathbf{k})$ but only a rapid variation in the vicinity of $\mathbf{k}_F$.

The case of interacting electrons at finite temperatures is much more interesting. The energy levels are now broadened and shifted by the self-energy $\Sigma=\Sigma'+i\Sigma''$, with $G^{-1}(\mathbf{k},\omega)=\omega-\epsilon_{\mathbf{k}}-\Sigma(\mathbf{k},\omega)$. Thus the spectral function is given by

$$A(\mathbf{k},\omega)=\frac{1}{\pi}\frac{|\Sigma''(\mathbf{k},\omega)|}{[\omega-\epsilon_{\mathbf{k}}-\Sigma'(\mathbf{k},\omega)]^2+[\Sigma''(\mathbf{k},\omega)]^2}. \qquad (4)$$

The electronic dispersion is now given by tracking the peak of the spectral function. We define a Fermi-surface crossing by the **k** point at which the spectral function peak crosses the chemical potential ($\omega=0$)

$$\Re e\, G^{-1}(\mathbf{k}_F,\omega=0)=0. \qquad (5)$$

This definition agrees with the standard definition of the Fermi surface at $T=0$ in an interacting Fermi system, which can be described by Landau's Fermi-liquid theory.[24] For this case, there is an additional (equivalent) characterization of the Fermi surface in terms of a discontinuity in $n(\mathbf{k})$ at $T=0$.

However, it should be stressed that the discussion above in terms of the spectral function is very general, and not necessarily limited to Fermi liquids. We propose to use the above definition in terms of the peak of the spectral function, which is valid even at finite temperatures, and use it to define the Fermi surface for high T_c superconductors, even though the spectral peaks above T_c are too broad for the system to qualify as a Landau Fermi liquid.[6] The question of whether the $T=0$ momentum distribution shows any singularity or not, cannot be addressed experimentally, since at $T=0$ one is not in a normal state but rather a broken symmetry state. We do find, however, that the Fermi surface we experimentally determine above T_c encloses a number of electrons that are consistent with the Luttinger count[24] of $(1+x)$, where x is the hole doping.

Let us now discuss in detail how these characterizations of the Fermi surface will be used in practice to determine $\mathbf{k}_F$. The first method (a) is simply to look at the dispersion of the peaks of the measured EDC's and determine from this when the peak position crosses the chemical potential. There are two caveats to this method. First, the peak of the EDC does *not* in general coincide with the peak of the spectral function $A(\mathbf{k},\omega)$. As can be seen from Eq. (2), if there is a broad spectral function A centered about $\omega=0$, then the peak of the EDC will be at $\omega<0$, produced by the Fermi function chopping off the peak of A, in addition to resolution effects. This can readily be seen in the data, as will be discussed in
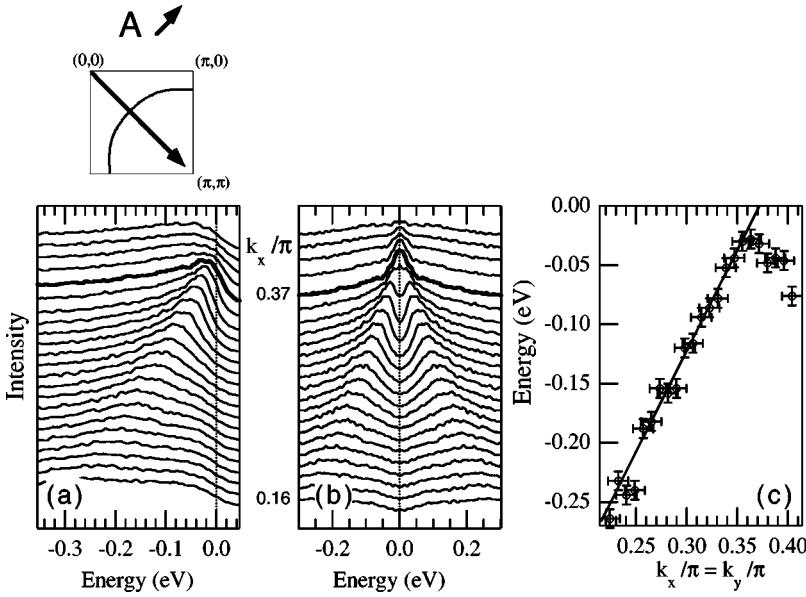
FIG. 5. Determination of the Fermi crossing along $(0,0) \rightarrow (\pi,\pi)$ in Bi2212-OD 88 K obtained at $h\nu = 22$ eV, $T = 180$ K: (a) EDC's with the state at the Fermi momentum shown in bold; (b) symmetrization of the EDC's in (a); (c) dispersion obtained from the data in (a).

connection with Fig. 5(c) below, and can be corrected for under favorable circumstances. The second problem with method (a) is that it may be difficult to use in cases where the dispersion is very weak, as for instance near the $(\pi,0)$ point in the cuprates. We should note that with sufficiently fine **k** sampling, these problems are minimized, as shown recently by us in Ref. 15. However, as we show here, even in the absence of such data, it is possible to make progress.

We turn to the symmetrization method (b), which allows us to overcome both the limitations of the method (a). This method was originally introduced by us[25] as a means of "dividing out the Fermi function" from the EDC and directly infer the spectral function A. In order to determine $A(\mathbf{k}_F, \omega)$ one had to assume particle-hole symmetry on a low-energy scale. However, we now use this idea for a different purpose, namely, Fermi-surface determination. As we show below we *do not need any assumptions about p-h symmetry to determine* $\mathbf{k}_F$.

For an arbitrary **k**, we define the symmetrized ARPES intensity by

$$I_{\text{sym}}(\mathbf{k}, \omega) = I(\mathbf{k}, \omega) + I(\mathbf{k}, -\omega) \qquad (6)$$

For simplicity, we will ignore resolution effects here, and we use Eq. (2) on the right-hand side of Eq. (6). (The effect of energy and momentum resolution convolutions are discussed in the Appendix.) Our goal is to use I_{sym} to determine $\mathbf{k}_F$ at which A has a maximum at $\omega = 0$.

Analyzing the symmetrized intensity about $\omega = 0$, for any **k**, we see that $dI_{\text{sym}}/d\omega(\omega = 0) = 0$ and

$$\left. \frac{d^2 I_{\text{sym}}}{d\omega^2} \right|_{\omega=0} = \left. \frac{d^2 A}{d\omega^2} \right|_{\omega=0} - \frac{1}{T} \left. \frac{dA}{d\omega} \right|_{\omega=0}. \qquad (7)$$

For $\mathbf{k} \neq \mathbf{k}_F$, the second term on the right-hand side dominates at sufficiently low temperature. For an *occupied* state, it is easy to see that $dA/d\omega(\omega = 0) < 0$, so that $d^2 I_{\text{sym}}/d\omega^2(\omega = 0)$ is positive. Thus the symmetrized intensity will exhibit a local minimum, or a dip, at $\omega = 0$ for an occupied k state.

Conversely, for an *unoccupied* state $dA/d\omega(\omega = 0) > 0$, and the left-hand side of Eq. (7) is negative, leading to a local maximum in the symmetrized intensity at $\omega = 0$. Precisely at $\mathbf{k} = \mathbf{k}_F$, the spectral function has a maximum at $\omega = 0$. Thus the second term of Eq. (7) vanishes and the first term leads to $d^2 I_{\text{sym}}/d\omega^2(\omega = 0) < 0$, yielding a peak or local maximum in I_{sym} at $\omega = 0$.

In practice, symmetrization is used to determine the Fermi crossing $\mathbf{k}_F$ as follows. We symmetrize *all* EDC's along a cut in **k** space and identify $\mathbf{k}_F$ as the boundary in momentum space between where symmetrized data have a dip (local minimum) versus a peak (local maximum) at $\omega = 0$. This will be demonstrated in detail below, where the symmetrization estimate for $\mathbf{k}_F$ from ARPES data is also compared with other estimates, wherever possible, and found to agree.

Before turning to the data (in the next section), we show one example of a simulation, which illustrates symmetrization with resolution effects included. In Fig. 6 we plot symmetrized intensities for five **k** points along a certain cut in **k** space. We see that for *occupied* states, corresponding to the first two **k** points, the spectral functions peak at $\omega < 0$, and thus the corresponding symmetrized spectra show dips, or local minima, at $\omega = 0$. As $\mathbf{k}_F$ is approached, this minimum gets shallower. At $\mathbf{k}_F$, half the peak is being chopped off in the EDC. Therefore, upon symmetrization, it is completely restored. (Note we did not build in any matrix element effects in this simulation). Once you go beyond $\mathbf{k}_F$, as in the last two curves, more than half the peak is chopped off in the EDC, so there is an intensity drop in the symmetrized plot. In addition, one observes that unoccupied states continue to exhibit a peak at $\omega = 0$ in their symmetrized intensity in Fig. 6, as can be understood from the preceding discussion.

We note that symmetrization makes precise, or formalizes, a rough criterion often used by ARPES practitioners: at $\mathbf{k}_F$ a vertical line through the chemical potential intersects the midpoint (half the maximum intensity) of the leading edge of the EDC.[26] It should be emphasized that a very precise determination of the chemical potential ($\omega = 0$) is necessary to determine $\mathbf{k}_F$ via symmetrization.[27]
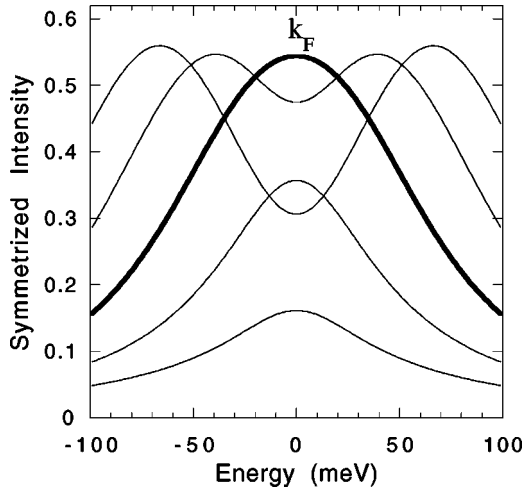
FIG. 6. Plot of symmetrized intensities obtained from simulation for five **k** points ($\phi=2.5°-6.5°$) for a $\theta=14°$ cut in **k** space (ΓM geometry). The curve closest to k_F ($\equiv 4.6°$) is shown in bold. The dispersion was chosen from the tight-binding fit of Ref. 33. A (constant) linewidth broadening of 50 meV was used, with a Gaussian energy resolution of $\sigma=15$ meV, and a 1° radius **k** window. A Fermi function with $T=14$ K was used, and matrix elements were ignored. Using these parameters, the five EDC's were generated and then plotted after symmetrization.

Finally we turn to another method (C) devised by us,[21,28] based on the sum rule Eq. (3) relating the energy-integrated ARPES intensity to the momentum distribution $n(\mathbf{k})$. In principle, the rapid variation of $n(\mathbf{k})$ offers a very direct probe of the Fermi surface, which is again not restricted to Fermi liquids. (The $T=0$ momentum distribution for known non-Fermi liquid systems, such as Luttinger liquids in one dimension, shows an inflection at $\mathbf{k}_F$.) In several cases we have demonstrated the usefulness of this method in our earlier work[21,28] where $\mathbf{k}_F$ was estimated from the location of $\max|\boldsymbol{\nabla}_{\mathbf{k}} n(\mathbf{k})|$. The same method has also been successfully used later by other authors.[29,30]

However, there is an important caveat to keep in mind: one does not measure $n(\mathbf{k})$, but rather the integrated intensity

$$I(\mathbf{k}) = \int_{-\infty}^{+\infty} d\omega I(\mathbf{k},\omega) = I_0(\mathbf{k};\nu;\mathbf{A}) n(\mathbf{k}). \qquad (8)$$

Potential problems for Fermi-surface determination can, and do, arise from the **k** dependence of prefactor $I_0(\mathbf{k};\nu;\mathbf{A})$ due to ARPES matrix elements. In Secs. VII and VIII below, we discuss in detail how to distinguish **k** dependencies of the integrated intensity coming from $n(\mathbf{k})$ and from the matrix elements.

To conclude our discussion of Fermi-surface criteria, we note that we will restrict ourselves here to the normal state. We will *not* discuss in this paper the notion of the ''minimum gap locus''[28,31] in a gapped state (either below T_c or in the pseudogap regime) which is a measurement of the underlying Fermi surface that got gapped out. We also mention, for completeness, two other methods of Fermi- surface determination, which we will not discuss in this paper. The first
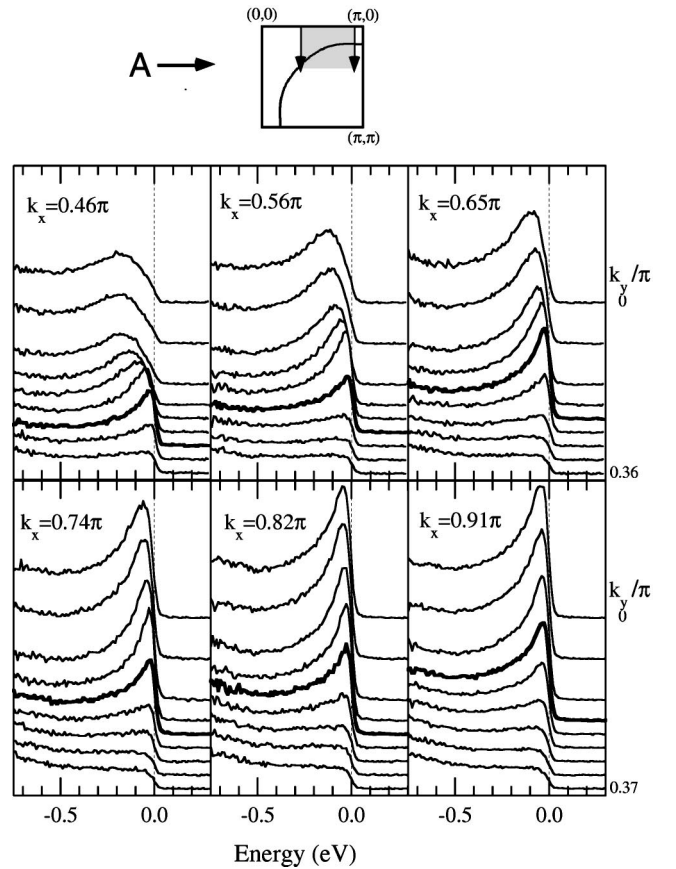
FIG. 7. EDC's from Bi2201-OD 23 K obtained at $h\nu=22$ eV, T$=25$ K along cuts perpendicular to the $(0,0)\rightarrow(\pi,0)$ direction, with k_x indicated in each panel.

one exploits the approximate sum rule[21] that $dn(\mathbf{k}_F)/dT=0$, i.e., the integrated intensity at $\mathbf{k}_F$ is independent of temperature. The second method uses the constant ω scan, or momentum distribution curve, as a function of **k**, at $\omega=0$; see Ref. 32.

VI. FERMI CROSSING FROM SYMMETRIZATION

We will show below that the symmetrization method provides a simple and general way of determining a Fermi crossing, even when the dispersion is very small. As discussed above, we will identify $\mathbf{k}_F$ as that **k** for which the symmetrized data *first* shows a clear peak at the chemical potential ($\omega=0$).

We begin with the simplest Fermi crossing along the zone diagonal, $(0,0)\rightarrow(\pi,\pi)$, where the electronic structure shows rapid dispersion. The data for a Bi2212-OD 88 K sample shown in Fig. 5(a), were obtained with an incident photon energy of 22 eV and polarization **A** parallel to the $(0,0)-(\pi,-\pi)$ axis. These $T=180$ K spectra are extremely broad, and not at all consistent with a Fermi-liquid picture.[6,32] We first determine the Fermi crossing $\mathbf{k}_F$ using the dispersion of the observed peak. In Fig. 5(c) we plot the observed peak positions of the data in (a). One can see that in the narrow **k** interval plotted in Fig. 5(c), the dispersion is linear over much of the range, deviating from linearity due to
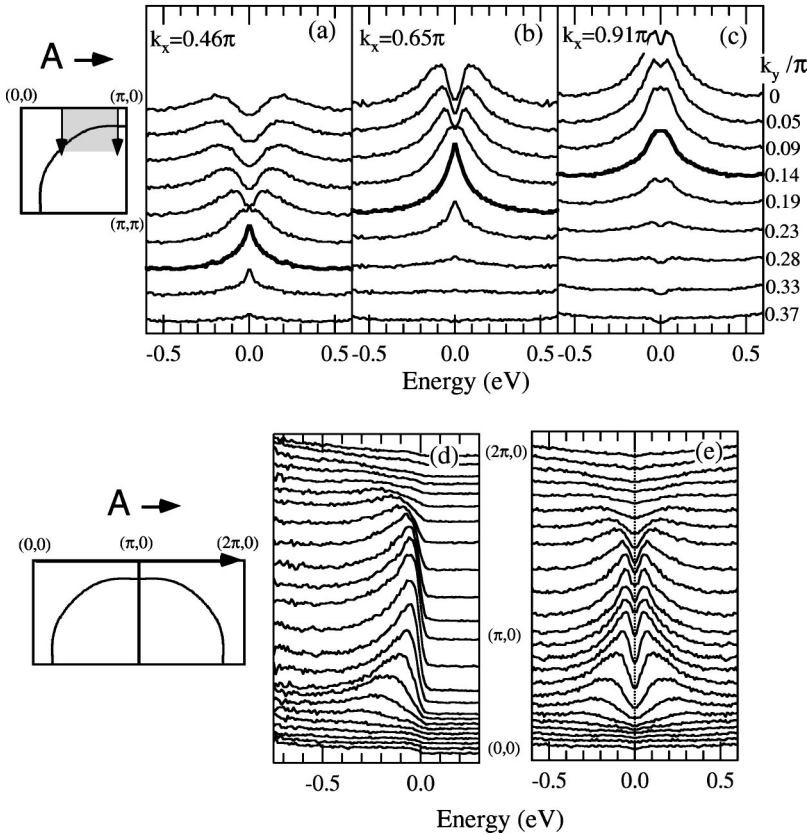
FIG. 8. (a)–(c) Symmetrization of selected data in Fig. 7. (d) EDC's along the $(0,0) \rightarrow (2\pi,0)$ direction; (e) symmetrization of the EDC's in (d), showing no Fermi-surface crossing.

the effect of the Fermi function (as discussed above). The extrapolation of the linear part crosses the chemical potential at $\mathbf{k}=(0.375\pi,0.375\pi)$, which is then the estimated $\mathbf{k}_F$ from the dispersion.

In Fig. 5(b) we plot the symmetrized intensities $I_{sym}(\mathbf{k},\omega)$ obtained from the data of Fig. 5(a). From this we see that the inferred spectral function is peaked at $\omega=0$ and also at $\mathbf{k}=(0.37\pi,0.37\pi)$. We thus find, that in this case, the dispersion and symmetrization methods give identical $\mathbf{k}_F$ estimates.

In the following we will first look at the simpler case of Bi2201. In the Pb-doped Bi2201 compounds, there are no observable complications arising from umklapp bands as in oxygen-doped Bi2201 or Bi2212 (which is discussed in more detail in Sec IX). We now move along the Fermi surface in Fig. 7, where the plotted data were obtained for an OD 23 K sample with an incident photon energy of 22 eV and polarization **A** parallel to the $(0,0)-(\pi,0)$ axis. One can observe a clear trend; as the $(\pi,0)-(\pi,\pi)$ line is approached, the dispersion becomes very small. In the vicinity of the $(\pi,0)$ it becomes very difficult to use the dispersion criterion to determine $\mathbf{k}_F$. Nevertheless, symmetrized data provide completely unambiguous results as can be seen from Fig. 8. From the top panels Figs. 8(a), 8(b), and 8(c) one can determine precisely the Fermi crossing from the **k** point at which the spectral function inferred from symmetrized data first peaks at the chemical potential.

Two points should be noted about the $\mathbf{k}_F$ estimate from symmetrization. First, just before approaching $\mathbf{k}_F$ from the occupied side, we expect that the symmetrized data will show two peaks and a small dip, which would be broadened

by resolution into a rather flat topped symmetrized spectrum. Second, there should be an intensity drop upon crossing $\mathbf{k}_F$ in the symmetrized spectrum, assuming that the matrix elements are not strong functions of **k**. Both of these effects are clearly seen in the data.

It is equally important to be able to determine the *absence* of a Fermi crossing in a cut in **k** space as shown in Figs. 8(d) and 8(e). In this respect, the raw data along $(0,0)-(\pi,0)$ $-(2\pi,0)$ is quite difficult to interpret, since the "band" flattens while approaching $(\pi,0)$, and remains extremely close to E_F. Nevertheless, it is simple to see that at no point along this cut do the symmetrized data show a peak centered at E_f, thus establishing the absence of a Fermi crossing along this cut.

The important conclusion from this discussion is that for Pb-doped Bi2201, one can continuously follow a Fermi-surface contour, which traces a hole barrel centered at (π,π). Analysis of a large set of data using the symmetrization method allows an unambiguous determination of the Fermi-surface crossing with high accuracy, even in the unfavorable case of broad peaks with weak dispersion.

VII. MATRIX ELEMENTS

As discussed at the end of Sec. V, great care must be used in determining a Fermi crossing from the integrated intensity, which is the momentum distribution $n(\mathbf{k})$ multiplied by the prefactor $I_0(\mathbf{k};\nu;\mathbf{A})$. A loss of integrated intensity as a function of **k** can arise either from a drop in $n(\mathbf{k})$ related to a Fermi crossing, or from the **k** dependence of the matrix elements in I_0.
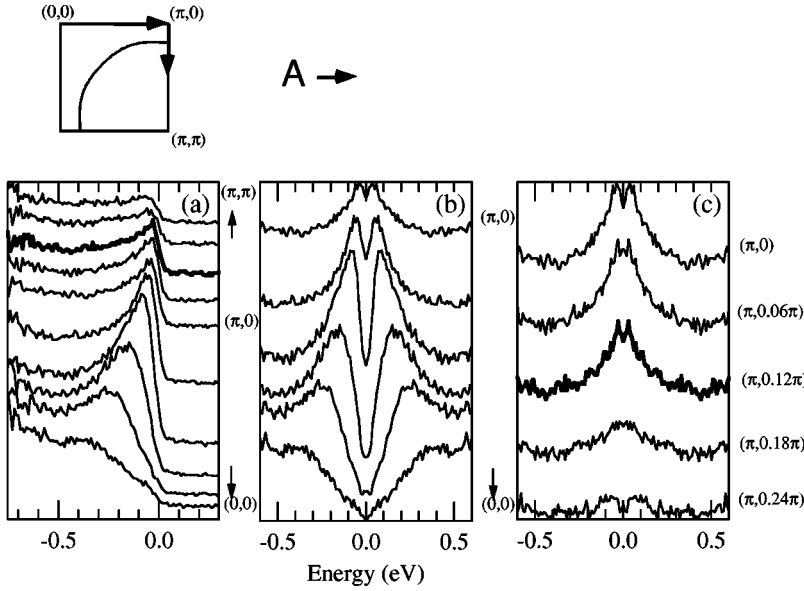
FIG. 9. Determination of the Fermi crossing in Bi2201-OD 23 K at $h\nu=34$ eV, T$=25$ K. (a) EDC's along the $(0,0)\rightarrow(\pi,0)\rightarrow(\pi,\pi)$ directions. Symmetrized data (b) along $(0,0)\rightarrow(\pi,0)$ showing no Fermi crossing and (c) along $(\pi,0)$ $\rightarrow(\pi,\pi)$ showing a clear Fermi crossing.

One possibility is to have *a priori* information about the matrix elements from electronic structure calculations.[34] But as we now show, even in the absence of such information, one can experimentally separate the effects of a strong **k** variation of the matrix element from a true Fermi surface crossing. The basic idea is to exploit the fact that by changing the incident photon energy one only changes the ARPES matrix elements and not the momentum distribution of the initial states.

In Fig. 9(a) we shows cuts along $(0,0)-(\pi,0)$ and $(\pi,0)-(\pi,\pi)$ obtained at a photon energy of 34 eV (to be contrasted with the data in the previous two figures for the same sample at 22 eV). The symmetrized data are shown in Figs. 9(b) and 9(c) from which we see results entirely consistent with those obtained at 22 eV. There is no Fermi crossing along $(0,0)-(\pi,0)$ since the symmetrized data in Fig. 9(b) never show a peak at $\omega=0$. Turning to the $(\pi,0)-(\pi,\pi)$ direction, the symmetrized data [Fig. 9(c)] do show a Fermi crossing occurring at k$=0.12\pi$, in agreement with the data obtained at 22 eV ($k=0.14\pi$).

However, there is an important difference between the data sets at 22 eV and 34 eV photon energies, which can be appreciated in Fig. 10, where the integrated intensity along the two directions is displayed. While at 22 eV, the maxi-

mum intensity occurs close to $(\pi,0)$ and decreases both towards $(0,0)$ and (π,π), the data taken at 34 eV show a strong depression of intensity on approaching $(\pi,0)$, resulting in a shift of the intensity maximum away from $(\pi,0)$. This loss of intensity cannot be interpreted as a Fermi crossing, since at no point in the symmetrized data from $(0,0)$ $\rightarrow(\pi,0)$ (Fig. 9) is there a peak centered at $\omega=0$. (In fact, this loss of intensity close to $(\pi,0)$ is responsible for the reduced signal-to-noise ratio in the 34 eV data in Fig. 9 compared with the 22 eV data in Figs. 7 and 8).

We would like to attribute this loss in intensity around $(\pi,0)$ at 34 eV, and in fact the entire variation seen in Fig. 10(a), to strong **k**-dependent matrix element effects. A direct proof is found from the data; the EDC's at the same point in the Brillouin zone obtained at the two different photon energies exhibit exactly the same lineshape, i.e., one can be rescaled onto the other as shown in Fig. 10(b).

We emphasize that the results of Fig. 10 imply that the photon energy dependence of the ARPES data is *not* a k_z dispersion effect. If this were the case, different incident photon energies would be probing initial states with different k_z values. However, the scaling of Fig. 10(b) proves that it is the *same* two-dimensional (k_z independent) initial state, which is being probed, and the photon energy dependence
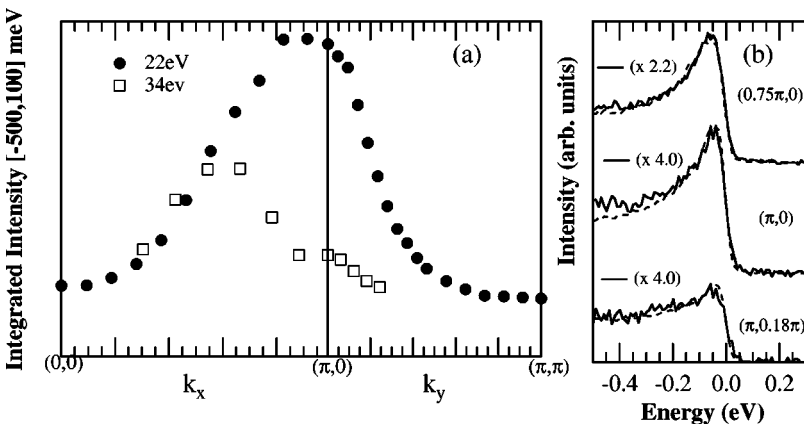
FIG. 10. Bi2201-OD 23 K, (a) Integrated intensity at $h\nu=22$ and 34 eV along the $(0,0)$ $\rightarrow(\pi,0)\rightarrow(\pi,\pi)$ directions. (b) Comparison of the ARPES lineshape measured at 22 (dashed lines) and 34 eV (solid lines) at three different **k** points.
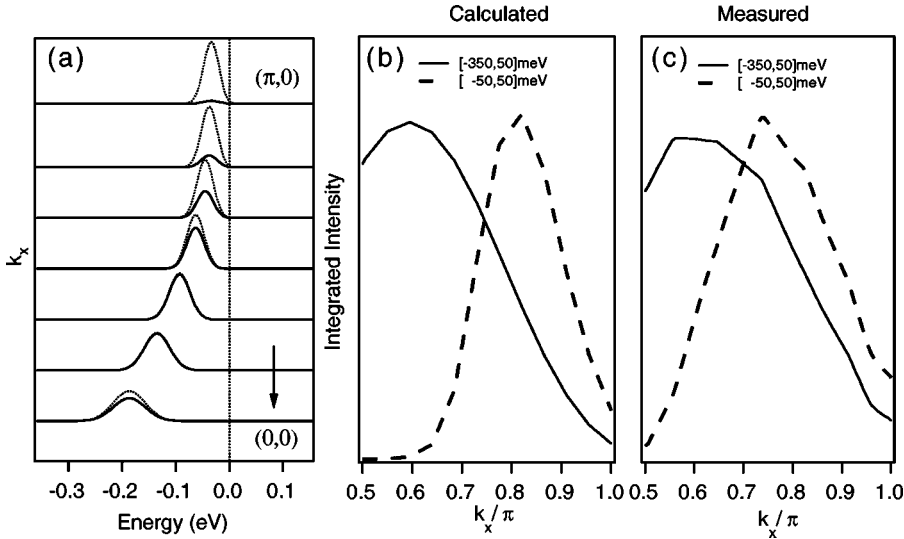
FIG. 11. (a) Model calculation of the dispersive band along the $(0,0) \rightarrow (\pi,0)$ direction, assuming no (dashed lines) and strong (solid lines) k dependence of the matrix elements. The variation of the matrix element observed in Fig. 10 at 34 eV is simulated by a $\sin^4(0.6k_x)$ function. (b) Integrated intensity over a narrow $(-50,+50$ meV) and wide $(-350,+50$ meV) energy range using the model calulation shown in (a). (c) Integrated intensity over the same integration ranges as in (b) obtained experimentally on Bi2201-OD 23 K at $h\nu = 34$ eV.

arises from the different final states that the matrix element couples to.

To further illustrate the role of matrix elements, we present a model calculation and compare it with the data of Fig. 10. The purpose of this exercise is to determine whether or not the data are consistent with a matrix element variation with **k**. In Fig. 11(a) we use dotted lines to show the dispersion of a model ARPES spectrum along $(0,0)$ to $(\pi,0)$, where the ''band'' approaches E_F near $(\pi,0)$ without a Fermi crossing. (The dispersion is chosen from the tight-binding fit of Ref. 33 to ARPES data on Bi2212 for illustrative purposes even though we will compare it to data on Bi2201). The full curves in Fig. 11(a) show the effect of the matrix element variation on the model spectra, simulated by $I_0(\mathbf{k}) = \sin^4(0.6k_x)$ along $(0,0)$ to $(\pi,0)$. This is a simple phenomenological matrix element (squared), which satisfies the following properties: it vanishes at the Γ point, as dictated by symmetry, and then has nonmonotonic behavior along Γ-M with a peak away from the M point, similar to that obtained by detailed band-structure calculations.[34] We emphasize that, beyond this, no deep meaning should be attached to the simple analytical form used.

Figure 11(b) shows the momentum dependence of the intensity integrated over the (large) energy range of -350 to $+50$ meV as a solid line, and over the (narrow) energy range -50 to $+50$ meV as a dashed line. One can see that this simple example shows remarkable agreement with the measured intensity using the same integration ranges, shown in Fig. 11(c). These results are easy to understand. The data with the large integration range first increase in intensity simply following the matrix element variation. The data with integration over a small energy range however shows a different intensity behavior. They start to increase for k values higher than 0.65π because only when the peak is closer to the Fermi energy does it contribute to the integrated intensity. It then again decreases rapidly because of the strong decrease of the matrix element, as in the previous case.

However, not recognizing the role of matrix elements, some authors have ascribed the differences between the 22 eV and 34 eV photon energy data to additional ''mysteri-

ous'' states around $(\pi,0)$.[12] We feel that there is no necessity to invoke such states or to assert changes in Fermi-surface topology with photon energy. In conclusion, all our data on Bi2201, when analyzed using the methods described above, indicate a large Fermi surface centered around (π,π) *independent of the photon energy.*

VIII. THE MOMENTUM DISTRIBUTION

Despite the matrix element issues discussed above, it is nevertheless interesting to study the integrated intensity [Eq. (8)] for a dense data set in the entire zone. The results obtained are shown in Fig. 12 for an OD 0 K sample. In the top panels, Figs. 12(a) and 12(c), we show the integrated intensity $I(\mathbf{k})$ around the $(\pi,0)$ point obtained at two different photon energies: 22 eV and 28 eV, respectively. In the lower panels, Figs 12(b) and 12(d), we plot the magnitude of the logarithmic gradient $|\nabla_\mathbf{k}I(\mathbf{k})|/I(\mathbf{k})$, which emphasizes the rapid changes in the integrated intensity. The logarithmic gradient filters out the less abrupt changes in the matrix elements and helps to focus on the intrinsic variations in $n(\mathbf{k})$. This can be seen from the fact that the integrated intensities in the top panels are quite different for 22 eV and 28 eV, while the logarithmic gradients are much more similar.

The Fermi surface can be clearly seen as two high intensity arcs curving away from the $(\pi,0)$ point. Modulo matrix element effects, the results obtained at the two different photon energies, are quite similar. Moreover, the Fermi surface estimated by this method is in good agreement with the one obtained from the symmetrization analysis above.

IX. THE FERMI SURFACE OF Bi2212

We now turn to Bi2212 where, in addition to all the issues discussed above for Bi2201, there is an added complication due to the presence of umklapp bands arising from the superlattice modulation with wave vector $\mathbf{Q} = (0.21\pi, 0.21\pi)$ in the BiO layers. Another difference with Bi2201, which we will not address here, is that Bi2212 has a CuO_2 *bilayer*; we only mention that no bilayer splitting is observed in the
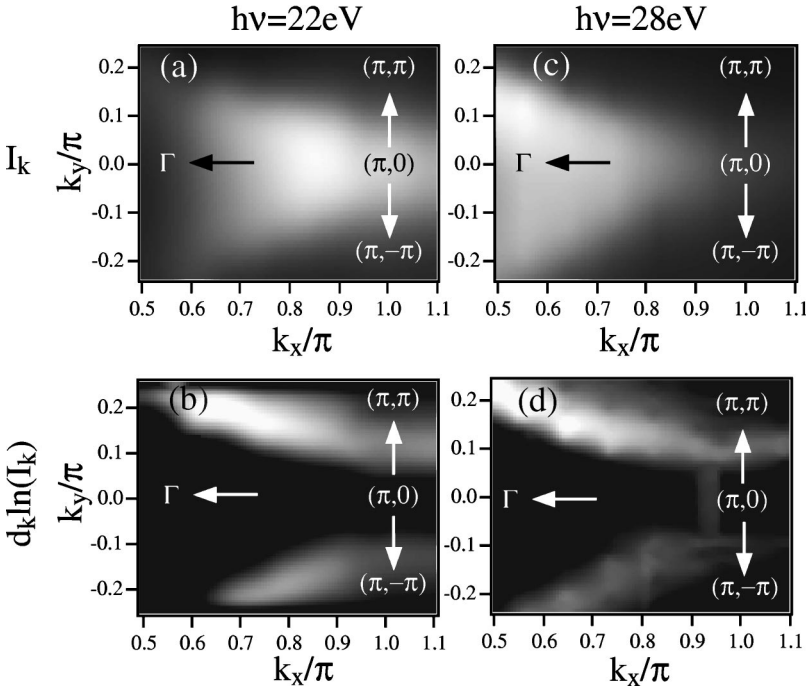
FIG. 12. Bi2201-OD 0 K: (a) and (c) Integrated intensity (over -310 to $+90$ meV) $I(\mathbf{k})$ measured at $h\nu=22$ and 28 eV, and T$=16$ K around the $(\pi,0)$ point. Notice that the intensity maximum depends strongly upon the photon energy $h\nu$.(b) and (d) Corresponding gradient of the logarithm, $|\nabla_{\mathbf{k}}I(\mathbf{k})|/I(\mathbf{k})$, the maxima (white) which corresponds to Fermi crossings and clearly show that, *independent of the photon energy*, the Fermi surface consists of a hole barrel centered around (π,π).

ARPES data on Bi2212 as discussed in detail in Ref. 5. In this section we will first review the effect of the superlattice on the electronic structure probed by ARPES, emphasizing the usefulness of polarization selection rules. In an earlier letter,[5] we had shown data along the principal axes of Bi2212. Here we present cuts throughout the Brillouin zone, analyzed using the symmetrization and integrated intensity methods discussed above, together with a detailed study of the photon energy dependence of the matrix elements. All of these new data and their analysis substantially strengthen our earlier conclusions. (See also Ref. 15.)

In Fig. 13 we show the electronic structure from EDC peaks [in Fig. 13(c)] and Fermi surface crossings [in Fig. 13(b)] determined from data at incident photon energies of 19 and 22 eV for an OD 87 K sample.[5] The dark lines in the bottom panel of Fig. 13 are a fit of the intrinsic planar CuO$_2$ electronic structure $\epsilon_{\mathbf{k}}$, which we call the ''main band;'' see Refs. 5 and 33 for details. The lighter lines are simply obtained by plotting $\epsilon_{\mathbf{k}\pm\mathbf{Q}}$, where $\mathbf{Q}$ is the superlattice vector, and it is very important to note that these lines provide an excellent description of the data points that do not lie on main band. The data strongly suggest[35] that these additional ''umklapp bands'' arise due to diffraction of the outgoing photoelectron through the BiO superlattice, which leads to ''ghost'' images of the electronic structure at $\epsilon_{\mathbf{k}\pm\mathbf{Q}}$.

From the point of view of the present discussion of the Fermi crossings, it is very important to establish conclusively that the crossings $U4$ and $U5$ along $(0,0)$ to $(\pi,0)$, shown in the middle panel of Fig. 13, correspond to umklapp ''ghost'' images and *not* to the ''main band.'' The case of the Fermi crossing $U5$, closer to $(0,0)$, is unambiguous since it is just obtained from following the dispersion of the EDC peaks, which clearly fall on the umklapp band dispersion in Fig. 13(c).

The Fermi crossing $U4$ requires more care since the umklapp and main band dispersions are almost degenerate in the

vicinity of $(\pi,0)$. To disentangle these two contributions, we exploit the polarization selection rules discussed in Sec. IV. In Fig. 13(c), we use filled circle symbols to denote data obtained in an odd geometry, i.e., the initial state is odd
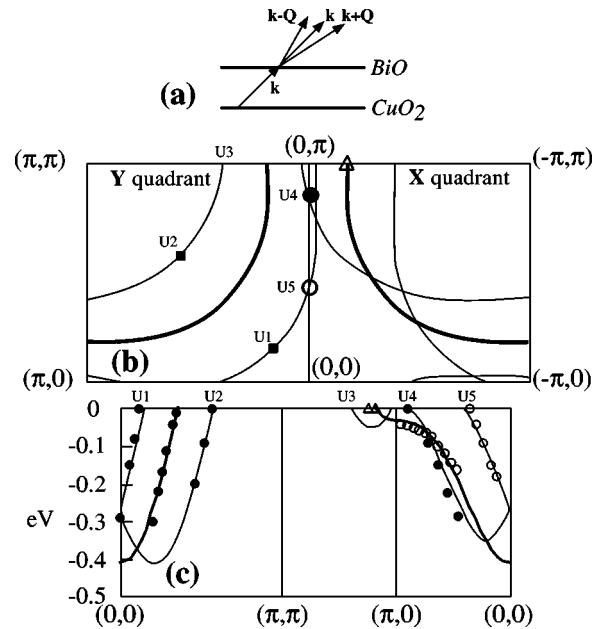
FIG. 13. (a) In the presence of the superstructure in the BiO layers, the outgoing electrons can be diffracted, thus giving rise to additional umklapp bands as shown in (b) and (c). (b) Main (thick) and umklapp (thin) Fermi surfaces. Selected Fermi crossings of the umklapp bands relevant for Figs. 14 and 15 are labeled from $U1$ to $U5$. (c) Dispersions obtained from earlier measurements on Bi2212-OD 87 K.[5] Filled circles denote data obtained in an odd polarization, i.e., the initial states odd under reflection in the corresponding mirror plane. Open circles denote even polarization, and open triangles correspond to a mixed polarization.
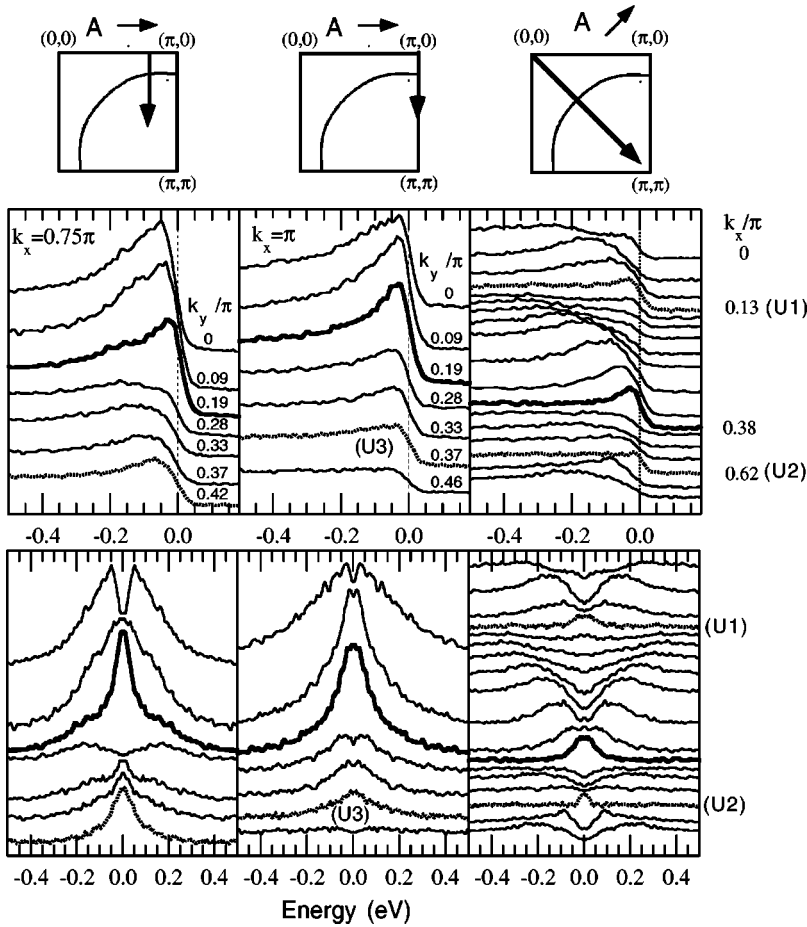
FIG. 14. Bi2212-OD 87 K. The top panels show the EDC cuts taken at $h\nu = 22$ eV, and T $= 100$ K together with the polarization geometry used. Various EDC's are shown in the middle panels, together with the corresponding symmetrized data in the lower panels. The curves corresponding to the Fermi crossing of the main and umklapp bands are shown with thick and broken lines, respectively. The labels $U1$ to $U3$ correspond to particular Fermi crossings of the umklapp band as shown in Fig. 13.

under reflection in the corresponding mirror plane, and open circles to denote even geometry. We see from the dispersion plotted in Fig. 13(c) that the main band signal is seen in the even geometry, since it is a dipole-allowed transition. (Actually, in this polarization, both the main and the umklapp bands should contribute, but in the 17–22 eV photon energy range, the main band intensity is much larger than that of the umklapps.) However in the odd polarization [filled circles along (0,0) to (π,0)] the main band is dipole forbidden and thus the weaker umklapp band, which does not have any symmetry restrictions here, dominates in this geometry. From the dispersion, and in particular the polarization geometry in which it is observed, we clearly see that the Fermi crossing $U4$ must be associated with the umklapp Fermi surface, and *not* with the main band.

Figure 14 shows various cuts at a photon energy of 22 eV for Bi2212-OD 87 K. The Fermi crossings are determined using the symmetrization method and the Fermi surface is found to be a hole barrel centered at (π,π). Notice that in each cut umklapp bands (broken lines) can be identified. The labels $U1$ to $U3$ correspond to particular Fermi crossings of the umklapp band as shown in Fig. 13. In particular along the (0,0) to (π,π) direction (right-side panels) the $U1$ and $U2$ crossings of the umklapp bands can be clearly observed.

These umklapp bands are also responsible for the $\omega = 0$ peaks observed in the symmetrized data beyond $\mathbf{k}_F$ in the other panels. The new data, obtained at much higher density in the zone, allows us to directly visualize the main Fermi

surface, together with the ghost Fermi surfaces due to umklapp bands, using the same procedure as in Fig. 12. The magnitude of logarithmic gradient $|\nabla_{\mathbf{k}}I(\mathbf{k})|/I(\mathbf{k})$ for Bi2212-OPT 90 K over part of the Brillouin zone in the Y quadrant (defined in Fig. 13) is shown in Fig. 15. From the intensity pattern in this plot, one can clearly see the main Fermi surface in the middle, which is a large holelike barrel, and also one of the umklapps ($U3$ in Fig. 13 notation). The other umklapps are weaker in intensity, but would be visible i n the figure if a log intensity scale had been used. It is quite satisfying to see indications of all the features deduced earlier (using other methods) in the plots obtained using the straightforward logarithmic gradient method.

The analysis of the photon energy dependence of the ARPES data in Bi2212 shows a similar trend to the one observed in Bi2201. As an example of this, we plot in Fig. 16 the photon energy dependence of the ratio $I(0.7\pi,0)/I(\pi,0)$ of the energy integrated intensity measured at $(0.7\pi,0)$ and $(\pi,0)$ for OD 88 K. Both these $\mathbf{k}$ points are inside the occupied part of the zone, and we would not expect the momentum distribution $n(\mathbf{k})$ to vary significantly from one point to the other. Thus, following Eq. (8), any significant deviation of this ratio from unity as a function of incident photon energy must be attributed to the matrix elements. While around 20 eV, $I(0.7\pi,0)/I(\pi,0)$ is close to unity indicating a small $\mathbf{k}$ dependence of the matrix elements in this part of the zone, the ratio peaks to about 2.5 at 38 eV, signaling the suppression of intensity around (π,0), similar
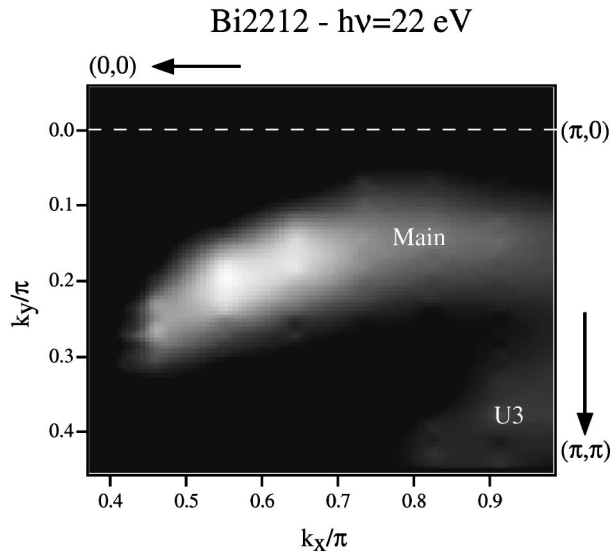
FIG. 15. Gradient of the logarithm of the integrated intensity (over -320 to $+80$ meV), $|\nabla_{\mathbf{k}} I(\mathbf{k})|/I(\mathbf{k})$, around $(\pi,0)$ for Bi2212-OPT 90 K taken at $h\nu=22$ eV. Note the large holelike Fermi-surface corresponding to the main band. In addition, the umklapp band ($U3$ in Fig. 13 notation) can be seen as well. The other umklapps are weaker in intensity, but would be visible if a log intensity scale had been used instead.

to what is seen in Bi2201. Even more interesting is the observation that around 54 eV the $I(0.7\pi,0)/I(\pi,0)$ becomes much *smaller* than one. Figure 16 illustrates once more how dangerous it would be to infer a Fermi crossing from intensity variations alone.

We have further observed[15] that at photon energies close to 30 eV, where the main band is strongly suppressed around $(\pi,0)$, the superlattice contributions are in fact strongly enhanced in this region. The reason is that these superlattice
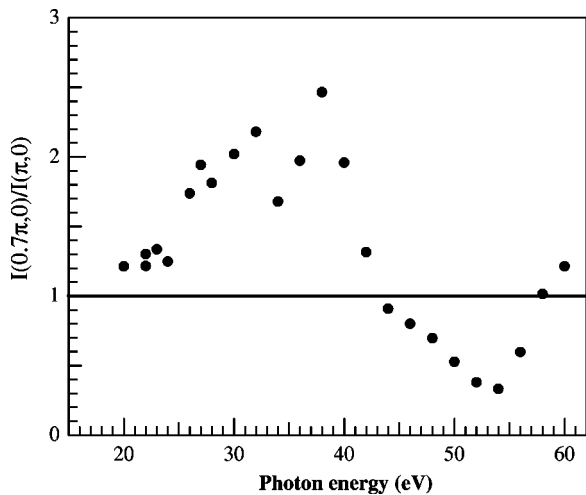
FIG. 16. Photon energy dependence of the integrated intensity ratio (over -600 to $+200$ meV) $I(0.7\pi,0)/I(\pi,0)$ of Bi2212-OD 88 K. The ratio is near unity at 20 eV, increases at 30 eV to two and larger, and decreases at 54 eV to less than one-half. This figure illustrates how dangerous it would be to infer a Fermi crossing from intensity variations only.

intensities originate from regions of reciprocal space where the matrix elements are less suppressed.

To summarize, it is very important that the superlattice contributions be differentiated from the main band using polarization selection rules, and all Fermi crossings carefully checked by a combination of symmetrization analysis together with careful studies of the integrated intensities as shown above.

X. CONCLUSIONS

In this paper we have carefully enunciated the criteria to be used in determining the Fermi surface from ARPES data. We have illustrated these ideas using data on two high T_c copper oxide based materials, Bi2201 and Bi2212. However we believe that these methods should prove to be useful for a large class of quasi-2D materials.

The high T_c materials are hard to analyze because of the absence of sharp quasiparticle peaks in their normal state, and anomalously weak dispersion in parts of the zone. Nevertheless, the symmetrization method discussed in this paper is able to deal with both these issues. It effectively removes the Fermi function from the EDC and determines $\mathbf{k}_F$ as that point in $\mathbf{k}$ space at which the spectral function peaks at the chemical potential.

It is very useful to supplement this analysis with studies of the momentum distribution, however one has to be very careful about matrix element effects. We show that by analyzing data at different incident photon energies, one can unambiguously distinguish between the loss of integrated intensity arising from matrix element variations from that due to genuine structure in $n(\mathbf{k})$. In this connection we have also shown the usefulness of studying the gradient of the logarithm of the integrated intensity.

We emphasize that not recognizing the role of matrix elements can lead to paradoxical conclusions such as changes in Fermi-surface topology with photon energy, which of course makes no sense. Some authors have ascribed the differences between the 22 eV and 34 eV photon energy data to additional states around $(\pi,0)$.[12,13] We find that there is no necessity to invoke such states.

Bi2212 has an additional complication arising from the effect of the BiO superlattice modulation on the ARPES data. However, as we argue above, the Fermi-surface crossings arising from ''ghost'' images (superlattice umklapp bands) can be clearly differentiated from the intrinsic planar CuO_2 Fermi surface by exploiting polarization selection rules.

In conclusion, all our data on Bi2201 and Bi2212, when analyzed using the methods described above, indicate a single large Fermi surface centered around (π,π), *independent of the photon energy*.

APPENDIX: SYMMETRIZATION AND RESOLUTION

In this Appendix we discuss in detail the effect of experimental resolution on the symmetrization method. For simplicity, we discuss the elimination of the Fermi function from the EDC *at* $\mathbf{k}_F$, which requires an assumption of particle-hole symmetry. As discussed in Sect. V, no such assumption was required for the determination of $\mathbf{k}_F$ via symmetrization.

Symmetrization was first introduced by us in Ref. 25 and used extensively for studying the self-energy in Ref. 27. The main result

$$I_{\text{sym}}(\mathbf{k}_F,\omega) = I(\mathbf{k}_F,\omega) + I(\mathbf{k}_F,-\omega) = I_0 A(\mathbf{k}_F,\omega) \tag{A1}$$

follows immediately from Eq. (2) by using the identity

$$f(-\omega) = 1 - f(\omega). \tag{A2}$$

obeyed by the Fermi function, together with the assumption of particle-hole symmetry at low energies (ω less than few times the temperature):

$$A(\mathbf{k}_F,\omega) = A(\mathbf{k}_F,-\omega). \tag{A3}$$

Let us now see how symmetrization works in the presence of finite energy and momentum resolutions. For clarity of presentation, we discuss these one at a time, although both can be trivially treated together. With a finite-energy resolution, Eq. (2) is generalized to

$$I(\mathbf{k},\omega) = I_0 \int_{-\infty}^{+\infty} d\omega' R(\omega-\omega') f(\omega') A(\mathbf{k},\omega'), \tag{A4}$$

where R is typically taken to be a Gaussian. Using $R(\omega-\omega') = R(\omega'-\omega)$ and Eqs. (A2) and (A3), we can easily see that

$$I_{\text{sym}}(\mathbf{k}_F,\omega) = I(\mathbf{k}_F,\omega) + I(\mathbf{k}_F,-\omega)$$

$$= I_0 \int_{-\infty}^{+\infty} d\omega' R(\omega-\omega') A(\mathbf{k}_F,\omega'). \tag{A5}$$

Thus symmetrization succeeds in removing the effect of the Fermi function from inside the convolution integral.

Next consider the effect of a small, but finite, $\mathbf{k}$ window. In its presence, Eq. (2) is replaced by

$$I(\mathbf{k},\omega) = I_0 f(\omega) \sum{}' A(\mathbf{k}',\omega), \tag{A6}$$

where Σ' is shorthand for summation over $\mathbf{k}'$ within the window centered about $\mathbf{k}$. We ignore the $\mathbf{k}$ variation of the prefactor I_0 within this small window, which allows us to pull it out of the sum. Next we need to extend our particle-hole symmetry assumption to $\mathbf{k}$'s slightly away from $\mathbf{k}_F$. We require

$$A(\epsilon_{\mathbf{k}},\omega) = A(-\epsilon_{\mathbf{k}},-\omega) \tag{A7}$$

valid for $|\omega|$ and $|\epsilon_{\mathbf{k}}|$ both less than a few tens of meV. Note that we have rewritten the first argument of the spectral function as $\epsilon_{\mathbf{k}}$, which can be linearized in the vicinity of $\mathbf{k}_F$ as $\epsilon_{\mathbf{k}} \simeq \mathbf{v}_F \cdot \delta\mathbf{k}$ where $\delta\mathbf{k} = (\mathbf{k}-\mathbf{k}_F)$. The symmetrized intensity is thus given by $I_{\text{sym}}(\mathbf{k}_F,\omega) = I_0 f(\omega) \Sigma' A(\mathbf{v}_F \cdot \delta\mathbf{k},\omega) + I_0 f(-\omega) \Sigma' A(\mathbf{v}_F \cdot \delta\mathbf{k},-\omega)$. We assume a *symmetric* window, so that if $\mathbf{k}_F + \delta\mathbf{k}$ is within the window, then so is $\mathbf{k}_F - \delta\mathbf{k}$. Thus we can rewrite the second term as $\Sigma' A(\mathbf{v}_F \cdot \delta\mathbf{k},-\omega) = \Sigma' A(-\mathbf{v}_F \cdot \delta\mathbf{k},-\omega)$, which on using Eq. (A7) is given by $\Sigma' A(\mathbf{v}_F \cdot \delta\mathbf{k},\omega)$. Finally, using Eq. (A2), we get

$$I_{\text{sym}}(\mathbf{k}_F,\omega) = I_0 \sum{}' A(\mathbf{k}',\omega). \tag{A8}$$

Combining the arguments that led to Eqs. (A5) and (A8), we see that the symmetrization procedure works in the presence of both energy and momentum resolution. In our previous work[25,27] we had used this procedure to analyze data at $\mathbf{k}_F$ mostly in the pseudogap and superconducting states.

*Present Address: Laboratory for Neutron Scattering, ETH Zurich and Paul Scherrer Institut, CH-5232 Villigen PSI, Switzerland.

†Present Address: Department of Physics, University of Wales Swansea, Swansea SA2 8PP, United Kingdom.

[1] See, e.g., S. Huefner, *Photoemssion Spectroscopy* (Springer-Verlag, Heidelberg, 1996).

[2] J.C. Campuzano, H. Ding, M.R. Norman, H.M. Fretwell, M. Randeria, A. Kaminski, J. Mesot, T. Takeuchi, T. Sato, T. Yokoya, T. Takahashi, K. Kadowaki, P. Guptasarma, D.G. Hinks, Z. Konstantinovic, Z.Z. Li, and H. Raffy, Phys. Rev. Lett. **64**, 2308 (1990).

[3] C.G. Olson, R. Liu, D.W. Lynch, R.S. List, A.J. Arko, B.W. Veal, Y.C. Chang, P.Z. Jiang, and A.P. Paulikas, Phys. Rev. B **42**, 381 (1990).

[4] Z.X. Shen and D. Dessau, Phys. Rep. **253**, 1 (1995).

[5] H. Ding, A.F. Bellman, J.C. Campuzano, M. Randeria, M.R. Norman, T. Yokoya, T. Takahashi, H. Katayama-Yoshida, T. Mochiku, K. Kadowaki, G. Jennings, and G.P. Brivio, Phys. Rev. Lett. **76**, 1533 (1996).

[6] A. Kaminski, J. Mesot, H. Fretwell, J.C. Campuzano, M.R. Norman, M. Randeria, H. Ding, T. Sato, T. Takahashi, T. Mochiku, K. Kadowaki, and H. Hoechst, Phys. Rev. Lett. **84**, 1788 (2000).

[7] K. Gofron, J.C. Campuzano, A.A. Abrikosov, M. Lindroos, A. Bansil, H. Ding, D. Koelling, and B. Dabrowski, Phys. Rev. Lett. **73**, 3302 (1994).

[8] D.S. Dessau, Z.-X. Shen, D.M. King, D.S. Marshall, L.W. Lombardo, P.H. Dickinson, A.G. Loeser, J. DiCarlo, C.-H Park, A. Kapitulnik, and W.E. Spicer, Phys. Rev. Lett. **71**, 2781 (1993).

[9] P. Aebi, J. Osterwalder, P. Schwaller, L. Schlapbach, M. Shimoda, T. Mochiku, and K. Kadowaki, Phys. Rev. Lett. **72**, 2757

(1994); J. Osterwalder, P. Aebi, P. Schwaller, L. Schlapbach, M. Shimoda, T. Mochiku, and K. Kadowaki, Appl. Phys. A: Solids Surf. **60**, 247 (1995).

[10] J. Mesot, M.R. Norman, H. Ding, and J.C. Campuzano, Phys. Rev. Lett. **82**, 2618 (1999).

[11] N.L. Saini, J. Avila, A. Bianconi and A. Lanzara, M.C. Asensio, S. Tajima, G.D. Gu, and N. Koshizuka, Phys. Rev. Lett. **79**, 3467 (1997).

[12] Y.-D. Chuang, A.D. Gromko, D.S. Dessau, Y. Aiura, Y. Yamaguchi, K. Oka, A.J. Arko, J. Joyce, H. Eisaki, S.I. Uchida, K. Nakamura, and Yoichi Ando, Phys. Rev. Lett. **83**, 3717 (1999).

[13] D.L. Feng, W.J. Zheng, K.M. Shen, D.H. Lu, F. Ronning, J.-i. Shimoyama, K. Kishio, G. Gu, D. Van der Marel, and Z.-X. Shen, cond-mat/9908056 (unpublished).

[14] T. Takeuchi, H. Ding, J.C. Campuzano, T. Yokoya, T. Takahashi, I. Chong, T. Terashima, and M. Takano, Physica C **282-287**, 999 (1997).

[15] H. Fretwell, A. Kaminski, J. Mesot, J.C. Campuzano, M.R. Norman, M. Randeria, T. Sato, R. Gatt, T. Takahashi, and K. Kadowaki, Phys. Rev. Lett. **84**, 4449 (2000).

[16] S.V. Borisenko, M.S. Golden, S. Legner, T. Pichler, C. Dürr, M. Knupfer, J. Fink, G. Yang, S. Abell, and H. Berger, Phys. Rev. Lett. **84**, 4453 (2000).

[17] We note that the intensity may not be the same on either side of the $(\pi,0)$ point because of either matrix element effects or the direction of incident light.

[18] Such plots have been extensively used by T. Takahashi and coworkers; see, e.g., T. Sato *et al.*, J. Phys. Chem. Solids **59**, 1912 (1998).

[19] J. Hermanson, Solid State Commun. **22**, 9 (1977).

[20] For this discussion it is perhaps simpler to imagine changing the photon polarization, keeping the detector fixed. In the actual experiment, however, it is the photon polarization that is fixed and the detector is moved when checking dipole selection rules.

[21] M. Randeria, H. Ding, J-C. Campuzano, A. Bellman, G. Jennings, T. Yokoya, T. Takahashi, H. Katayama-Yoshida, T. Mochiku, and K. Kadowaki, Phys. Rev. Lett. **74**, 4951 (1995).

[22] The background contribution is however significant at higher binding energies. For recent discussions of the background in the high T_c materials, see L.Z. Liu, R.O. Anderson, and J.W. Allen, J. Phys. Chem. Solids **52**, 1473 (1991); M.R. Norman, M. Randeria, H. Ding, and J.C. Campuzano, Phys. Rev. B **59**, 11191 (1999); and Ref. 23

[23] M.R. Norman, H. Ding, H. Fretwell, M. Randeria, and J.C. Campuzano, Phys. Rev. B **60**, 7585 (1999).

[24] A.A. Abrikosov, L.P. Gorkov, and I.E. Dzyaloshinski, *Methods of Quantum Field Theory in Statistical Physics* (Dover, New York, 1963).

[25] M.R. Norman, H. Ding, M. Randeria, J.C. Campuzano, T. Yokoya, T. Takeuchi, T. Takahashi, T. Mochiku, K. Kadowaki, P. Guptasarma, and D.G. Hinks, Nature (London) **392**, 157 (1998).

[26] This midpoint criterion works only for sufficiently broad EDC's, however symmetrization is more general in that it works independent of linewidth. Moreover, in gapped states, e.g., below T_c or in the pseudogap regime, one finds a local minimum at $\omega = 0$ in the symmetrized data (see Refs. 25 and 27) even when one is at a $\mathbf{k}$ location coinciding with the normal (ungapped) state $\mathbf{k}_F$. In this sense, symmetrization also demonstrates the destruction of a Fermi surface crossing in gapped states.

[27] M.R. Norman, M. Randeria, H. Ding, and J.C. Campuzano, Phys. Rev. B **57**, R11 093 (1998), and Ref. 23

[28] J.C. Campuzano, H. Ding, M.R. Norman, M. Randeria, A.F. Bellman, T. Yokoya, T. Takahashi, H. Katayama-Yoshida, T. Mochiku, and K. Kadowaki, Phys. Rev. B **53**, R14 737 (1996).

[29] Th. Straub, R. Claessen, P. Steiner, S. Hüfner, V. Eyert, K. Friemelt, and E. Bucher, Phys. Rev. B **55**, 13 473 (1997).

[30] M. Schabel, C.-H. Park, A. Matsuura, Z.-X. Shen, D.A. Bonn, Ruixing Liang, and W.N. Hardy, Phys. Rev. B **57**, 6107 (1998).

[31] H. Ding, M.R. Norman, T. Yokoya, T. Takeuchi, M. Randeria, J.C. Campuzano, T. Takahashi, T. Mochiku, and K. Kadowaki, Phys. Rev. Lett. **78**, 2628 (1997). In this paper a leading edge analysis was employed to determine the Fermi crossing. This method also yields accurate results, but for simplicity we do not discuss it here.

[32] A. Kaminski, M. Randeria, J.C. Campuzano, M.R. Norman, H. Fretwell, J. Mesot, T. Sato, T. Takahashi, and K. Kadowaki, Phys. Rev. Lett. **86**, 1070 (2001).

[33] M.R. Norman, M. Randeria, H. Ding, and J.C. Campuzano, Phys. Rev. B **52**, 615 (1995).

[34] A. Bansil and M. Lindroos, J. Phys. Chem. Solids **59**, 1879 (1998); Phys. Rev. Lett. **83**, 5154 (1999).

[35] There are two different interpretations of the umklapp ''bands'': (a) a final-state effect involving diffraction of the outgoing photoelectron off the BiO superlattice, or (b) an initial state effect caused by the BiO superlattice perturbing the CuO$_2$ electronic structure. There are several pieces of evidence in favor of interpretation (a). First, polarization selection rules are obeyed for the $(0,0)-(\pi,0)$ mirror plane, and this would not be a mirror plane if the initial state electronic structure was affected by the superlattice. Second, the intensities of the main band compared with the umklapp bands in the vicinity of $(\pi,0)$ argue strongly in favor of interpretation (a); see Ref. 15.